

## Jetting of a shear banding fluid in rectangular ducts

Paul F. Salipante,<sup>1,\*</sup> Charles A. E. Little,<sup>2</sup> and Steven D. Hudson<sup>1</sup><sup>1</sup>*National Institute of Standards and Technology, Polymers and Complex Fluids Group,  
Gaithersburg, Maryland 20899, USA*<sup>2</sup>*National Institute of Standards and Technology, RF Electronics Group, Bolder, Colorado 80305, USA*

(Received 14 December 2016; published 14 March 2017)

Non-Newtonian fluids are susceptible to flow instabilities such as shear banding, in which the fluid may exhibit a markedly discontinuous viscosity at a critical stress. Here we report the characteristics and causes of a jetting flow instability of shear banding wormlike micelle solutions in microfluidic channels with rectangular cross sections over an intermediate volumetric flow regime. Particle-tracking methods are used to measure the three-dimensional flow field in channels of differing aspect ratios, sizes, and wall materials. When jetting occurs, it is self-contained within a portion of the channel where the flow velocity is greater than the surroundings. We observe that the instability forms in channels with aspect ratio greater than 5, and that the location of the high-velocity jet appears to be sensitive to stress localizations. Jetting is not observed in a lower concentration solution without shear banding. Simulations using the Johnson-Segalman viscoelastic model show a qualitatively similar behavior to the experimental observations and indicate that compressive normal stresses in the cross-stream directions support the development of the jetting flow. Our results show that nonuniform flow of shear thinning fluids can develop across the wide dimension in rectangular microfluidic channels, with implications for microfluidic rheometry.

DOI: [10.1103/PhysRevFluids.2.033302](https://doi.org/10.1103/PhysRevFluids.2.033302)

### I. INTRODUCTION

Complex fluids are characterized by a variety of rheometric tools that measure material functions, such as viscosity, normal stresses, viscoelastic moduli, etc. Capillary and slit rheometers have several advantages and disadvantages for measuring these properties. Such rheometers are simple and extremely accurate [1], and even non-Newtonian fluids are analyzed accurately with the procedure of Rabinowitsch [2]. Microfluidic approaches to capillary and slit rheometry are especially advantageous for a small sample volume [3] and depending on channel geometry permit access to high shear rates at low to modest Reynolds number [4,5]. In this paper, we will explore how channel geometry introduces complex flow behavior in strongly non-Newtonian fluids.

Wormlike micelles (WLMs), which are flexible elongated cylindrical aggregates self-assembled from surfactants, are examples of a very complex non-Newtonian fluid [6–8]. In an applied flow, a non-Newtonian response results in entanglement or disentanglement of these wormlike threads, structural alignment with the flow, and reversible breaking of the micelles [9]. In the limit of fast micelle breakage, the single-mode Maxwell model can be used to describe the linear viscoelastic response of the fluids at low frequencies, while a more detailed model is required to understand the full frequency response [10–13]. Above a semidilute concentration limit, a dramatic drop in viscosity occurs at a critical applied stress, indicating a transition to a different fluid microstructure [14]. This structural transition in the fluid accompanies a nonmonotonic stress response as a function of applied shear rate [15], so that multiple shear rate values are stable at a given stress. Rheological measurements provide values for the stress plateau and the shear rates that the plateau spans. These parameters are useful for understanding shear banding in more complex flow geometries.

In a shear flow with a constant applied shear rate, a shear banding fluid can separate into two and possibly more shear bands, where the local shear rate differs from the applied one. Shear banding

---

\*Corresponding author: paul.salipante@nist.gov

occurs when the fluid microstructure cannot stabilize to match the applied shear rate, and instead, the fluid responds by partitioning into shear rates with stable microstructures [16–19]. The location of the interface between the two shear bands has been shown to scale with the applied shear rate [20]. Even in shear flow, more complex behavior can arise; examples of this include velocity fluctuations in the vorticity direction and fluctuations in the shear rates or wall slip [21–28]. The stability of the interface between the two shear bands has also shown complex behavior [21,22,29,30] that can manifest in velocity variations along the vorticity direction [31,32] and in time-dependent flows [22,23,25,26,33,34].

While simple shear flow is a useful tool for rheological measurements, the common use of WLMs in applications that require pressure-driven flow motivates studying their behavior in capillaries and microfluidic channels. A variety of flow measurement techniques have been used to measure flow profiles of WLMs, including magnetic resonance imaging and fluorescent particle image velocimetry [27,35–40]. These studies have shown a dramatic increase in the volumetric flow within the capillary as a function of pressure, described as the “spurting” effect. The spurting flow is a consequence of the transition to pluglike flow, characterized by a high shear rate region near the wall and a relatively low shear rate region through the center of the channel. More complex behavior has also been observed in pressure driven flow, including temporal flow fluctuations [38,41–43].

Rheological measurements of shear banding fluids are particularly informative when combined with *in situ* structural measurements such as scattering, microscopy, birefringence, or other spectroscopic techniques. For such measurements, a slit geometry makes a straightforward connection to the principal directions of a rheometric flow. Rectangular microfluidic channels have been used to gather rheological data by fitting measured flow profiles across the narrow dimension to a one-dimensional flow model while also measuring flow-induced birefringence [40]. This approach assumes that the flow velocity gradient along the wide dimension of the channel is negligible. While this assumption is often valid for many fluids, non-negligible cross-stream gradients and instabilities have been observed in rectangular channels [21,44].

In this paper, we investigate dramatic departures from flow uniformity in rectangular channels. We show that the flow of WLM solutions can become unstable in rectangular channels and produce a localized and persistent high-velocity jet in the channel. Recently, similar jetting behavior of WLMs in microfluidic rectangular geometries was observed, although the origins of this behavior were not understood [44]. The jetting behavior, in which the local wall shear rate across the channel width varies dramatically, appears to be a complex manifestation of shear banding. Under these conditions, the Weissenberg-Rabinowitsch-Mooney analysis breaks down. We aim to show here that shear banding fluids produce persistent high-velocity jets in a variety of rectangular channels and through the use of numerical simulations provide evidence that the jetting behavior results from a redistribution of viscoelastic stresses.

We use a combination of three-dimensional (3D) and two-dimensional (2D) particle-tracking techniques to investigate the jetting flow behavior in rectangular microfluidic channels. Imaging methods, device fabrication, and theoretical background of the WLM solutions are discussed in Sec. II. In Sec. III we first present rheological measurements for the solution concentrations used in this study. The flow measurements of WLM over a range of flow conditions and in different channels are presented next. The results of the flow measurements are summarized in a phase diagram and compared to scaling arguments based on the wall shear rate. In Sec. IV, the experimental results are compared to finite volume simulations using the Johnson-Segalman viscoelastic model. The results of these simulations and the stress field that drives jet formation are then discussed.

## II. MATERIALS AND METHODS

### A. Fluid system and rheology

Wormlike micellar solutions of cetylpyridinium chloride (CPyCl) (Sigma-Aldrich) and sodium salicylate (NaSal) (Sigma-Aldrich) in Millipore water were prepared at a 5 to 3 molar ratio of CPyCl/NaSal. Three solution concentrations are used in experiments at room temperature (21 °C), denoted high, middle, and low concentration. Specifically, high is 100 mmol L<sup>-1</sup>CPyCl/60 mmol

$L^{-1}NaSal$ ; middle is  $75 \text{ mmol } L^{-1}CPyCl/45 \text{ mmol } L^{-1}NaSal$ ; and low is  $33 \text{ mmol } L^{-1}CPyCl/20 \text{ mmol } L^{-1}NaSal$ .

The rheological properties are measured using a stress-controlled MCR-301 (Anton Paar) with a cup and bob geometry. Frequency sweeps using small amplitude oscillatory shear over the range  $\omega = (0.02 \text{ to } 100) \text{ rad/s}$  and steady shear rate ramps over the range of  $\dot{\gamma} = (0.001 \text{ to } 2000) \text{ 1/s}$  are performed for each of the samples.

### B. Device fabrication

Three different methods are used to construct microfluidic devices: a fabrication process using SU-8 (an epoxy-based photoreactive polymer), which produces rigid channel geometries with well-controlled dimensions; a more rapid process for fabricating microfluidic channels using double-sided tape that can produce a wide range of aspect ratios; and rectangular glass capillaries used to provide channels with smooth surfaces on all sides and a consistent cross section.

The SU-8 microfluidic channels used in this paper are fabricated through a unique process. Multiple devices are fabricated on a single  $7.62 \text{ cm}$ ,  $500 \mu\text{m}$  thick, fused silica (FS) wafer, with each device consisting of a single channel. SU-8 3050 was first spin-coated and patterned on the FS wafer to form the walls of the channels. The SU-8 thickness was measured to be approximately  $20 \mu\text{m}$ . The FS wafer with patterned SU-8 is then waxed face down to a carrier wafer. Laser ablation is used to etch fluid inlets and outlet ports through the backside of the wafer. The wafer is then diced into individual microfluidic devices and removed from the carrier wafer. A separate  $150 \mu\text{m}$  thick quartz cover slip is coated with  $2 \mu\text{m}$  of SU-8 2002. The microfluidic devices are placed on a hot plate at  $80 \text{ }^\circ\text{C}$ , above the glass transition temperature of the uncured SU-8. Cover slips are placed SU-8 side down on the microfluidic devices. Firm pressure is applied to the coverslip while on the hotplate forcing the uncured SU-8 to flow. The uncured SU-8 solidifies after removing the now fully enclosed microfluidic channels from the hotplate. The device is subsequently exposed with UV light through the coverslip side with the same pattern as the previous layer. After the exposure and a postexposure bake, the two layers of SU-8 are chemically bonded together, and the channels are fully sealed. The excess unexposed  $2 \mu\text{m}$  of SU-8 within the channel is removed with repeated washes with SU-8 developer and isopropanol. Quick connect bond ports are then added to the inlet and outlets using a two-component epoxy.

The optics used for the measurement restrict the working distance to less than  $200 \mu\text{m}$ . The process produces microfluidic channels that do not require a fixture to apply external pressure to maintain the integrity of the channel, allowing for easy optical and fluidic access. In addition, all surfaces within the channel are rigid; the channel dimensions are not expected to vary with pressure. Both the wafer and coverslip that form the floor and ceiling of the channels respectively are extremely flat, which both helps with uniform flow within the channel and is necessary to produce a low-scattering optical path for the holographic microscopy method employed here.

Double-sided tape is used to make rectangular microfluidic channels by cutting either  $50 \mu\text{m}$  thick tape (3M 9628B) or  $350 \mu\text{m}$  thick tape with a die cutting machine (Silhouette Cameo) and sandwiching the tape between a microscope glass slide and a  $(24 \times 50) \text{ mm}$  cover glass. Holes are drilled in the glass slide about  $4 \text{ cm}$  apart, and fluid ports are attached with epoxy. The tape is cut in the desired channel pattern spanning the ports and placed on the glass slide. Channels constructed with a range of widths are cut to investigate the effect of channel aspect ratio (AR) on flow behavior.

Rectangular capillaries with two different cross-section geometries are used ( $50 \times 500) \mu\text{m}$  and  $50 \mu\text{m} \times 1 \text{ mm}$  (Vitrocom). The capillaries are first attached with epoxy across a glass slide. Fluid ports are then attached with epoxy to both the outside of the capillary and the side of the glass slide for mechanical support. After the epoxy is cured, the end of the capillary is broken and filed down to the level of the fluid port.

### C. Flow control

Flow is generated using a pneumatic pressure flow system (Fluigent MFCS) or a syringe pump (Harvard Apparatus). The volumetric flow control is analogous to a rate-controlled shear rheometer

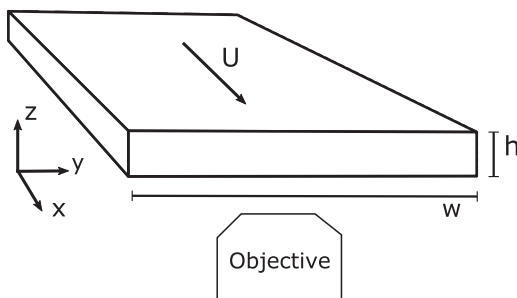


FIG. 1. Schematic of a rectangular microfluidic channel.

and a pressure-driven system comparable to a stress-controlled shear rheometer. Here the pressure drop is measured across the entire microfluidic circuit. With non-Newtonian fluids, it is difficult then to determine the pressure drop across a particular microfluidic component. The fluid resistance of each component changes as a function of shear rate, which depends on the component geometry. For the flow system used in this study, the microfluidic channel has the highest resistance of any flow component, such as tubing and connectors. Nevertheless, when a shear banding occurs in the microfluidic channel, the pressure drop across the channel can remain constant even as the total pressure across the flow system is increased. The pressure drop across each component in the flow system is estimated from the stress curve (see Supplemental Material [45]). This analysis is relevant for understanding the behavior of shear banding fluids in microfluidic devices and implies that both pressure-controlled flow and volumetric-controlled flow can produce the same flow behavior.

For all measurements, we record images after at least 10 minutes, for the flow field to reach steady state. The time to reach steady state varies with volumetric flow. At low flow rates, the fluid may take more than 10 minutes to reach a flow field that no longer varies with time. To test if the flow has reached a steady state, we compare two video recordings over a 10 minute period until there is no change in the mean velocity field measured with velocimetry.

#### D. Imaging

Images are generated using in-line digital holographic microscopy on an Olympus IX71 inverted microscope using a  $60\times$  water (1.2NA) objective; see Fig. 1. The channel is illuminated with a collimated beam from a 635 nm laser diode source (Thorlabs LDM635) mounted in the microscope lamphouse. Images are recorded using an Andor Zyla 5.5 sCMOS camera with  $4\times 4$  binning. A running median filter over the time sequence is used to make a background image, which is then used to normalize the entire sequence. The WLM solutions are seeded with  $1\ \mu\text{m}$  diameter fluorescent polystyrene particles at approximately 0.01 volume percent. The Rayleigh-Sommerfeld back-propagation method is used to reconstruct the 3D scattered light field, where the peaks in the scattered light field are related to the position of the particles [46]. The particle positions are determined by first applying an intensity threshold to the image, and then a Gaussian peak finding algorithm determines the particle location to a resolution of approximately 50 nm. The image-processing and particle-tracking operations are computed on a Tesla K20 GPU. The particle positions gathered over (500 to 1000) frames are processed using a particle-tracking velocimetry (PTV) algorithm that determines position-dependent velocities [47]. The uncertainty from the PTV algorithm are estimated from the standard deviation of velocity measurements made at the channel center. This measurement was repeated over a range of volumetric flows. The relative uncertainty in the velocity is estimated to be  $\pm 5.4\%$ .

The velocity field was examined also at lower resolution and wider field of view using epi-fluorescent imaging of the same polystyrene particles. The 2D flow field, i.e., without measuring the  $z$  position of a particle, is analyzed using an open-source particle image velocimetry (PIV) software

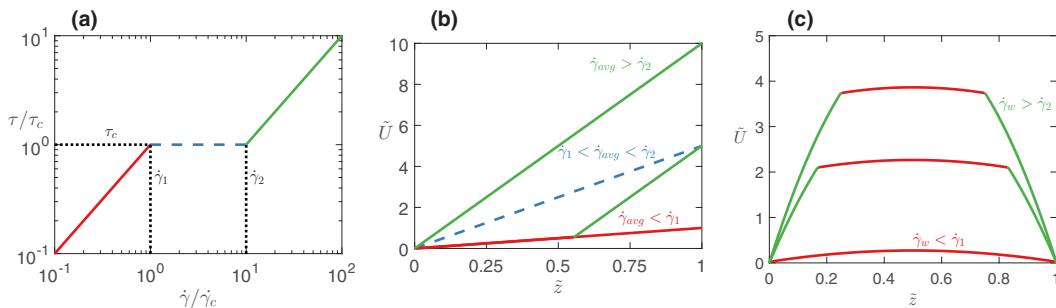


FIG. 2. (a) Schematic of the shear stress as a function of shear rate for a shear banding fluid. (b) Example of flow curves in a shear rate-controlled Couette flow. If the average shear rate is below the critical shear rate,  $\dot{\gamma}_1$ , or above the critical shear rate,  $\dot{\gamma}_2$ , there is a constant shear rate across the gap. When the average shear rate is between the two critical shear rates,  $\dot{\gamma}_1 < \dot{\gamma}_{app} < \dot{\gamma}_2$ , depicted by the dashed line, the fluid shear bands. (c) Schematic of Poiseuille flow showing parabolic flow when the wall shear stress is below the critical stress and pluglike flow when the wall shear stress exceeds the critical stress. Red lines indicate shear rates on the low shear rate branch, and green lines indicate shear rates on the high shear rate branch.

(PIVlab) [48,49]. In situations where there is no significant variation in the velocity field in the flow direction, PIV measurements are used to produce velocity profiles,  $U(y)$ , averaged along the flow direction. We estimate the uncertainty in the PIV measurements from the standard deviation of the velocity profile along the flow direction. PIV measurements are also used to measure the flow field, including its temporal development, at channel entrances.

### E. Theory

Shear banding arises in fluids that possess different microstructural states and drastically different viscosities. The appearance of shear banding in these fluids is dependent on the applied stress. From this simplified view, the stress curve has a low and high shear rate branch corresponding to high or low viscosity states, respectively [Fig. 2(a)]. As the stress is increased past some critical stress,  $\tau_c$ , in a stress-controlled Couette flow, the entire shear rate transitions from the low shear rate branch to a high shear rate branch. The two shear rates that correspond to the critical stress on each branch are defined as the critical shear rates,  $\dot{\gamma}_1$  and  $\dot{\gamma}_2$ ; see Fig. 2(a). The flow behavior differs in a rate-controlled Couette flow. If a shear rate,  $\dot{\gamma}_{app}$ , is applied between the two critical rates, the velocity field will become unstable and separate into shear bands. The two bands fill a fraction of the channel such that the two shear rates equal the applied average shear rate,  $\dot{\gamma}_{avg} = \dot{\gamma}_1\beta + \dot{\gamma}_2(1 - \beta)$ , where  $\beta$  is the fraction of fluid at  $\dot{\gamma}_1$  [Fig. 2(b)]. The stress remains constant at all shear rate between these the two critical shear rates [Fig. 2(a)].

While real systems exhibit more complex behavior, for example, shear thinning in the upper branch, the simplified description is useful for understanding flow of shear banding fluids in Poiseuille flow. In contrast to Couette flow, which at first order has a constant stress across the gap, planar Poiseuille flow results in a linear stress across the channel gap. Shear banding occurs when the wall shear stress exceeds the critical stress and the position of the interface between the low and high shear rate branch corresponds to the position of critical stress [Fig. 2(c)]. The transition of the wall shear rate from the low to high shear rate branch results in a continuous but sharp increase in volumetric flow, described as the spurting effect.

In contrast to planar Poiseuille flow, which ignores the channel sides and assumes no variation across the width of the channel, the flow behavior of shear banding fluids in rectangular channels presents additional complexity. Rectangular channels have variation in wall stress. Specifically, the wall stress is highest on the wide faces and smaller on the sides and corners. For example, for a Newtonian fluid in a high aspect ratio rectangular channel, the maximum wall stress at the sides is

approx 70% of the maximum along the top and bottom channel walls. Therefore, when stress in regions near the top and bottom surfaces of the channel exceeds the critical value for shear banding and the stress at the sides remains below this value, we anticipate a conundrum that might lead to more significant variations of flow across the width of the channel. We explore this conundrum with experiments and simulations.

It is essential to describe any deviations from planar Poiseuille flow, because planar Poiseuille flow is the basis of slit rheometry. Volumetric flow and pressure drop in a channel determine the relationship between shear rate and shear stress. Assuming an incompressible fluid, the flow in a rectangular channel is a function of the volumetric flow rate,  $Q$ , and the channel dimensions. The apparent shear rate in such case is

$$\dot{\gamma}_a^z = \frac{6Q}{wh^2}. \quad (1)$$

This equation assumes a parabolic flow profile and therefore cannot be used for a non-Newtonian fluid with shear rate-dependent viscosity. In the latter case, the wall shear rate can be determined with knowledge of the dependence of apparent shear rate  $\dot{\gamma}_a$  on stress with the Weissenberg-Rabinowitsch-Mooney (WRM) equation:

$$\dot{\gamma}_w = \frac{\dot{\gamma}_a}{3} \left[ 2 + \frac{d \ln \dot{\gamma}_a}{d \ln \tau_w} \right]. \quad (2)$$

This model is applicable even when shear banding occurs. The non-Newtonian response is captured by bracketed term in Eq. (2). The apparent shear rate is related to the wall shear stress by

$$\dot{\gamma}_a = \frac{3I}{\tau_w^2}, \quad (3)$$

where

$$I = \int_0^{\tau_w} \dot{\gamma} \tau d\tau. \quad (4)$$

The rheological results give a relationship between stress and shear rate. Here we use a smoothing spline to fit the shear rate as a function of stress, which can then be used to numerically integrate Eq. (4). The wall shear rate is to be compared to the critical shear rates defined in the previous section.

### III. RESULTS

#### A. Rheology

The frequency sweeps from small-amplitude oscillatory shear measurements, shown in Fig. 3, provide a number of important values that describe the viscoelastic fluid characteristics. The storage and loss moduli,  $G'$  and  $G''$ , demonstrate Maxwellian behavior at low frequencies. There is good agreement with a single-mode Maxwell model for the high and middle concentration systems, demonstrated by matching the ideal half-circle in Cole-Cole plot [Fig. 3(b)], signaling that chain breakage and recombination is faster than its relaxation by reptation [8].

The elastic modulus,  $G_0$ , and relaxation times,  $\lambda_M$ , are determined from fits to the Maxwell fluid model. The minimum value of  $G''/G_0$  provides an inverse measure of entanglements. Specifically, the reciprocal  $G_0/G'' \approx L/l_e$ , where average contour length is  $L$  and entanglement length is  $l_e$  [50]. Accordingly, entanglements per chain are approximately 5 for the middle concentration system and approximately 16 for the high concentration system. The entanglement length can be estimated from  $l_e \approx (k_b T/G_0)^{5/9}/l_p^{2/3}$ , where  $l_p$  is the persistence length, which is usually taken to be 15 nm [51]. We find entanglement lengths of  $l_e = 0.13 \mu\text{m}$  and  $l_e = 0.19 \mu\text{m}$  for the high and middle concentrations, respectively. From these values, the average contour length is approximately  $2.0 \mu\text{m}$  for the high concentration system and  $0.9 \mu\text{m}$  for the middle concentration system. The low concentration system is unentangled.

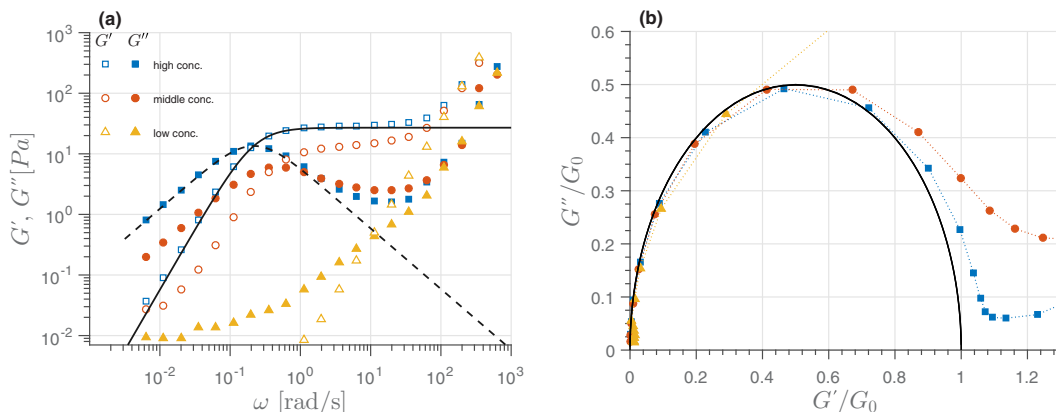


FIG. 3. (a) Measured storage and loss modulus for the three CPyCl/NaSal solution concentrations from small amplitude oscillatory measurements. Fits to a single-mode Maxwell model are shown for the high concentration system ( $G'$ : black solid line and  $G''$ : black dashed line). (b) Cole-Cole plots for the three system concentrations.

A stress plateau indicative of shear banding is evident in steady flow curves (Fig. 4) for the high and middle concentration systems while the low concentration system is monotonically increasing. The extent of the plateau region provides a definition for the lower and upper critical shear rates,  $\dot{\gamma}_1$  and  $\dot{\gamma}_2$ , which serve as a basis of comparison for the channel flow behavior. As discussed, the first critical shear rate corresponds to the onset of shear thinning behavior. This onset is related to the characteristic relaxation time of the fluid determined previously,  $\dot{\gamma}_1 \approx \lambda_M^{-1}$ , above which elastic stresses become relevant [4,11,16]. The upper critical shear rate is determined by finding the largest shear rate corresponding to the plateau stress. Increasing entanglements causes a reduction of  $\dot{\gamma}_2/\dot{\gamma}_1$  when chains are linear [52]. As a result, the largest relative jump in shear rate for a shear banding fluid occur just above the critical concentration where shear banding occurs. The middle concentration system has indeed a wider plateau region than the high concentration system. The rheometer progresses steadily through this plateau in part because the cup and bob geometry has a modest stress gradient from the outer to inner cylinder, according to differences in circumferences. The low concentration system does not exhibit a stress plateau, but the power-law shear thinning

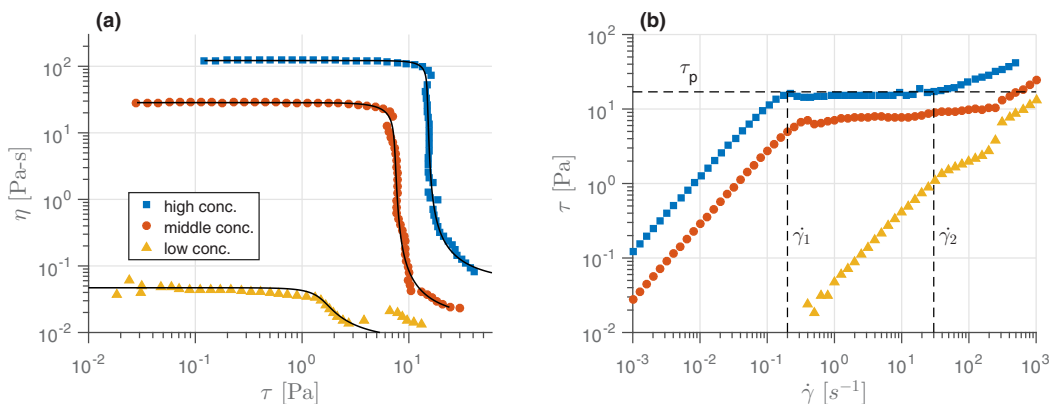


FIG. 4. (a) Viscosity and (b) shear stress plots for CPCI/NaSal solutions at different concentrations from steady shear measurements. The stress plateau and lower critical shear rates are shown for the high concentration system. Solid lines are fits to the Carreau-Yasuda model.

TABLE I. Table of parameter values determined from small amplitude oscillatory shear measurements.

Name	CPyCl/NaSal System [mmol/L]	$G_0$ [Pa]	$\lambda_M$ (s)	$G_0/G''_{\min}$
High	100/66	27	4.6	16
Middle	75/45	12	2.0	5
Low	33/20	0.6	0.1	–

behavior initiates at a critical shear rate, approximately  $\dot{\gamma}_1 = 50 \text{ s}^{-1}$ . While this critical shear rate does not correspond to a stress plateau, it is a useful reference for the onset of shear thinning. The properties from the Maxwell model fit for the three fluid systems are given in Table I.

A sharp decrease in viscosity is observed when viscosity is plotted as a function of stress [Fig. 4(a)]. The Carreau-Yasuda (CY) model is used to describe the shear-rate-dependent viscosity,

$$\eta(\dot{\gamma}) = \eta_\infty + (\eta_\infty - \eta_0) \left[ 1 - \left( \frac{\dot{\gamma}}{\dot{\gamma}_1} \right)^a \right]^{\frac{n-1}{a}}, \quad (5)$$

where  $\eta_0$  is the zero shear rate viscosity,  $\eta_\infty$  is the infinite shear rate viscosity,  $n$  is the power-law index, and  $a$  is a shape parameter. All three systems are described fairly well by the CY model over the range of shear rates measured, with the fitting parameters given in Table II. The steady shear rheology shown in Fig. 4(b) is used to determine the plateau stress and the critical shear rates, also given in Table II. The largest deviation from the CY model occurs for the low concentration system, which exhibits shear thickening at  $\tau = (3 - 7) \text{ Pa}$ . This has been attributed to shear induced structures that form at dilute concentration of WLM systems including the CPyCl/NaSal system [53]. For Poiseuille flow in a capillary, the shear-induced structures have been shown to result in lower shear rates near the wall where the shear-induced structures form and the highest shear rates are located at an intermediate radial position [41].

In contrast to simple shear flow, where the stress can be considered constant, Poiseuille flow in a rectangular duct has a linear stress profile across the channel height. The highest stress regions in channel are at the walls, and therefore as the volumetric flow is increased, the near wall region is the first to reach the critical stress,  $\tau_c$ . If the wall shear stress is below the critical value, the rheological results suggest quasi-Newtonian behavior. As the wall shear stress exceeds the critical value, a sharp increase in the wall shear rate leads to an abrupt transition to pluglike flow and a particularly blunted flow profile for shear banding fluids. We compare the flow profiles obtained from holographic microscopy to flow profile predictions using the CY model.

## B. Flow profile measurements

The rheological measurements for the low concentration system does not show a stress plateau, and therefore shear banding is not expected. Nevertheless, for shear rates that exceed the critical shear rate defined by the onset of strong shear thinning, we expect a transition from a quasi-Newtonian to pluglike flow. Figure 5 shows two representative flow cross sections in the  $(20 \times 200) \mu\text{m}$  channel (note the aspect ratio is not to scale). Numerically computed flow profiles are computed in MATLAB

TABLE II. Table of parameters from steady shear measurements.

System	$\tau_p$ [Pa]	$\eta_0$ [Pa-s]	$\eta_\infty$ [Pa-s]	$\dot{\gamma}_1$ [s <sup>-1</sup> ]	$\dot{\gamma}_2$ [s <sup>-1</sup> ]	$a$	$n$
High	16	121.8	0.057	0.12	50	4.3	0.02
Middle	8	28.4	0.015	0.25	200	2.8	0.02
Low	–	0.044	0.008	36.9	–	1.7	0.05

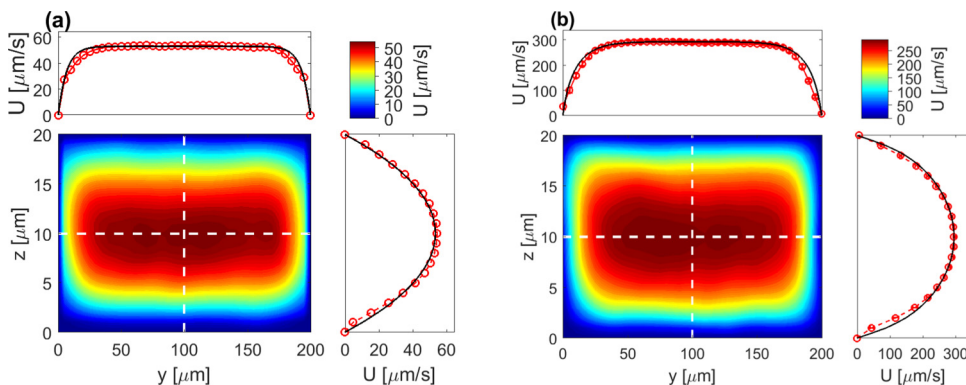


FIG. 5. Channel cross section velocity profiles for low concentration system in the (a) quasi-Newtonian, (b) pluglike regimes. Flow profiles in the  $y$  and  $z$  directions (red circles) are compared to numerically computed flow profiles using the CY model (black lines). (a) Parabolic flow across in the  $z$  direction and uniform flow in the  $y$  direction for volumetric flow  $Q = 0.14$  nl/s with estimated wall shear rate from Eq. (2)  $\dot{\gamma}_w^z = 11.0$  s $^{-1}$ . (b) A more pluglike flow is observed across the channel height and small gradients across the channel width for volumetric flow for  $Q = 0.77$  nl/s with estimated wall shear rate from Eq. (2)  $\dot{\gamma}_w^z = 68.4$  s $^{-1}$ .

using the CY model parameters to match the same volumetric flow in the channel. The experimental (shown in red circles) and numerical flow profiles (shown in black lines) are compared across the middle of the channel in  $z$  and  $y$  directions.

Figure 5(a) shows a flow profile of the low concentration system in the quasi-Newtonian regime. As expected from Newtonian flow behavior, a parabolic flow is observed across the channel height, and significant gradients in the  $y$  direction are limited to a distance of approximately  $1h$  from the side walls. There are no substantial flow gradients in the  $y$  direction across the center of the channel.

When the  $z$ -direction wall shear rate exceeds the critical shear rate,  $\dot{\gamma}_w^z > \dot{\gamma}_1$ , we observe a more blunted velocity profile across the channel height [see Fig. 5(b)] and velocity gradients that extend slightly further across the channel width. This effect is relatively minor for the low concentration system, which has a change in viscosity of  $\eta_0/\eta_\infty \approx 5$ . A fluid with a larger decrease in viscosity will produce a more blunted  $z$ -direction profile than that shown in Fig. 5, and the flow profile across the  $y$  direction may become nearly parabolic across the channel width.

When the flow is pluglike in the  $z$  direction, it will be useful to consider an apparent shear rate metric across the channel width as

$$\dot{\gamma}_a^y = \frac{6Q}{hw^2}. \quad (6)$$

This apparent shear rate is used to estimate a wall shear rate in the  $y$  direction,  $\dot{\gamma}_w^y$ , using Eq. (2). By analogy to the  $z$ -direction behavior, we expect that the flow profile across the channel width will be nearly parabolic when  $\dot{\gamma}_w^y < \dot{\gamma}_1$  and transition from parabolic to pluglike occurs when  $\dot{\gamma}_w^y > \dot{\gamma}_1$ . Indeed, this behavior is predicted by the CY model (see Fig. 6). While this metric [Eq. (6)] is limited in applicability, it does provide some intuition for how aspect ratio influences flow in strongly shear thinning fluids.

We compare the cross-section flow profile measurements for the high concentration system to predictions from the CY model at the same volumetric flow. At low volumetric flow, we observe a parabolic velocity profile across the channel height and a somewhat uniform flow across the channel width except for a slight increase in velocity near the side walls; see Fig. 6(a). The slight asymmetry in the flow profile across the channel width is likely a precursor to unstable flow in the channel. Despite this, the measured flow profiles match the quasi-Newtonian behavior predicted by the CY fairly well at this volumetric flow.

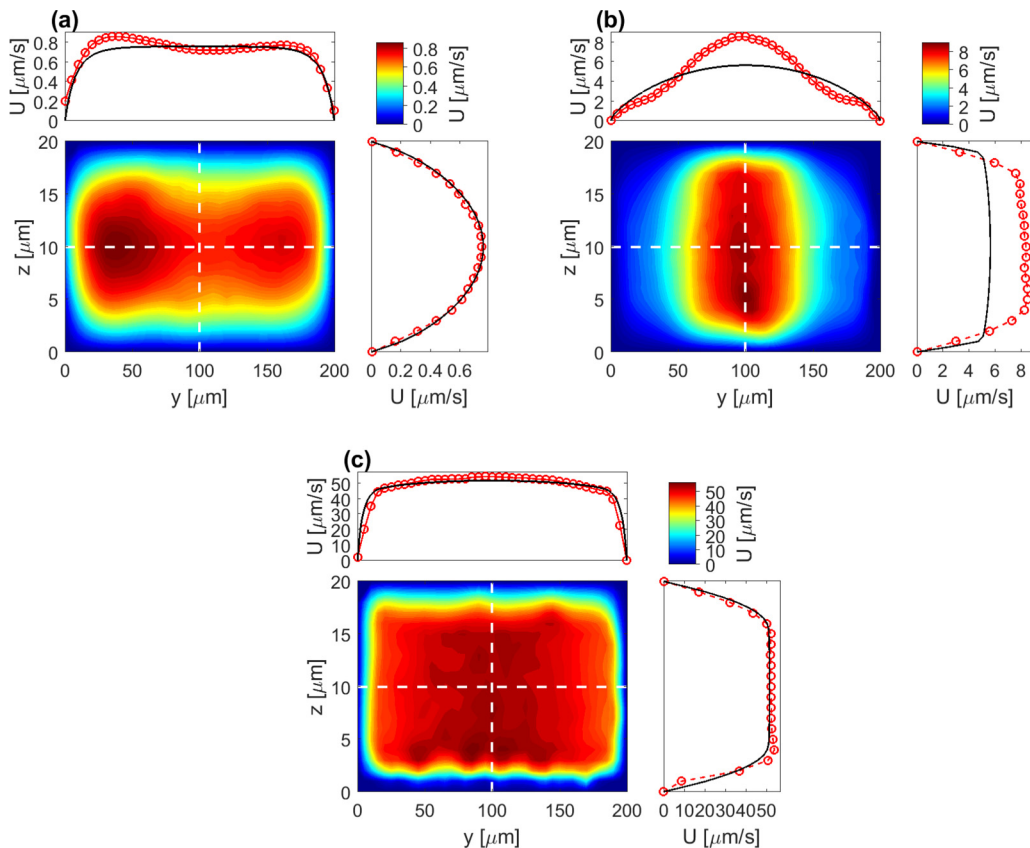


FIG. 6. Measured channel cross section velocity profiles for the high concentration system in the (a) quasi-Newtonian, (b) jetting, and (c) pluglike flow regimes. Flow profiles in the  $y$  and  $z$  directions (red circles) are compared to flow fields numerically computed using the CY model. (a) The quasi-Newtonian flow regime shows some variation in velocity across the channel width but predominantly parabolic flow across in the  $z$  direction  $Q = 0.002$  nl/s with estimated wall shear rate,  $\dot{\gamma}_w^z = 0.18$  s $^{-1}$ , from Eq. (2). (b) A jet in the middle of the channel is observed at intermediate volumetric flows,  $Q = 0.015$  nl/s with estimated wall shear rate,  $\dot{\gamma}_w^z = 12.3$  s $^{-1}$ , from Eq. (2). Pluglike flow is observed in the  $z$  direction, but jetting flow does not match the parabolic flow across the channel width predicted by the CY model. (c) At high volumetric flow, pluglike flow is observed across the entire channel cross-section  $Q = 0.160$  nl/s with estimated wall shear rate,  $\dot{\gamma}_w^z = 50.5$  s $^{-1}$ , from Eq. (2).

As the flow is increased, we observe that a stable high-velocity jet forms in the channel. This jet is characterized by a very sharp gradient in  $z$  near the top and bottom wall and near uniform velocity across the thin gap of the channel [Fig. 6(b)]. We observe the jetting behavior only in the high and middle concentration solutions, both of which show a stress plateau [Fig. 3(b)] indicative of shear banding. This suggests that the top and bottom wall bordering the jet are at the high stable shear rate branch,  $\dot{\gamma}_w > \dot{\gamma}_2$  [cf. direct measure of  $\dot{\gamma}_w^z$ ; Fig. 6(b)], while the remaining portion of the channel is in the low stable shear rate,  $\dot{\gamma}_w < \dot{\gamma}_1$ . The jet behavior is a clear deviation from the flow profile predicted from the CY model shown at the same volumetric flow in Fig. 6(b). The CY model predicts a blunted profile across the  $z$  direction and a parabolic profile across the  $y$  direction, as discussed above for the situation where  $\dot{\gamma}_w^y < \dot{\gamma}_1$  and  $\dot{\gamma}_w^z > \dot{\gamma}_1$ . The CY model's inability to fit the data exposes a need to model more than viscous effects alone. In a later section, we show that the Johnson-Segalman viscoelastic model provides a necessary description of the fluid stresses to replicate the jetting behavior.

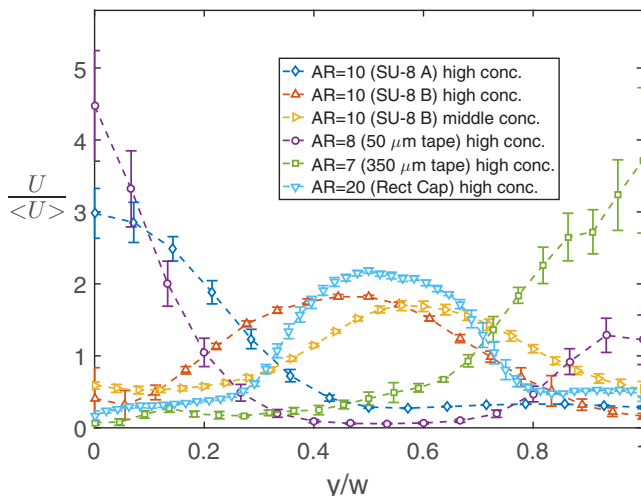


FIG. 7. Velocity profiles from PIV images of jetting flow in tape channels, SU-8 channels, and rectangular capillaries. The  $y$  position is normalized by the channel width and the velocity is normalized by the mean velocity. The jet forms along the side of the channels made from tape, both  $50\ \mu\text{m}$  tape ( $\text{AR} = 8$ ) and  $350\ \mu\text{m}$  tape ( $\text{AR} = 7$ ) and one SU-8 channel (SU-8 A) with sidewall defects. The jet forms in middle of channel in a rectangular capillary (Rect Cap) and another SU-8 channel (SU-8 B) without wall defects, shown for both high and middle concentrations. Error bars show the standard deviation of the velocity determined from PIV measurements.

At a higher volumetric flow, the width of jet increases until it fills the entire channel [Fig. 6(c)]. The flow profile is characterized as pluglike across both the channel height and width, and the flow profile returns to fitting the CY model. This suggests that the wall stress in both  $y$  and  $z$  directions is above the critical value, and the wall shear rates at all channel boundaries are in the high shear rate branch,  $\dot{\gamma}_w^z > \dot{\gamma}_2$  and  $\dot{\gamma}_w^y > \dot{\gamma}_2$ , at stable single-valued shear rates.

The jetting behavior appears distinct from the “spurting” flow observed in round capillaries and has been observed only in rectangular channels. We investigate the effect of channel construction and geometry on the jetting behavior in the following sections.

### C. Jetting characterization

Since jetting here accompanies the onset of shear banding, the jet is likely to form at the location of the largest stress in the channel. For a Newtonian fluid in a rectangular channel, this location is at the wall in the center of the channel, which suggests that the jet will always form there. In our experiments, however, the jet can form either near the channel center [as shown in Fig. 6(b)] or at the side walls, but the jet will repeatedly form in the same location for a given channel. We investigate how the location of the jet depends on the materials and construction of the channel.

Figure 7 compares the velocity profiles across the channel width for jetting flow in various channels using PIV. In SU-8 channels, the jets formed either in the center or at the side walls. The velocity profile shown for channel SU-8 A demonstrates a jet that forms along the side wall. Another SU-8 channel, denoted SU-8 B, produces jetting flow in the in the center of the channel (shown for both high and middle concentrations in Fig. 7). Any defects along the side wall may introduce an increase in the local stress at the sidewall. A slight misalignment of the SU-8 layers was observable in the SU-8 A channel but absent in the SU-8 B channel. The misalignment likely induces a stress concentration that triggers the jump to higher shear rates and jet formation. The effect of surface roughness and defects on the flow behavior of shear banding fluids has been shown to alter flow profiles in both Poiseuille and Couette flows [36,54]. In the case of pressure-driven flow

in rectangular capillaries, any irregularities at the side walls will cause a localized stress and jump in shear rate.

The effect of defects is more evident in channels constructed with tape, which have rough side walls as a result of cutting the tape. In all tape channels used for this study, the jets form along one or both walls in the tape channels. The flow in an  $AR = 8$  tape channel made using  $50\ \mu\text{m}$  thick tape shows jets on both sides of the channel (Fig. 7), although the jet along one side is faster than the jet along the other. Similar behavior was observed by Haward *et al.* in channels constructed from glass separated by metal spacers [44]. They observed a single jet located in the center of the channel that eventually split into two jets close to the side walls after approximately 1 hour.

To determine whether asymmetry in channel wall material drives the jetting behavior, we observed the flow of the high concentration solution through rectangular capillaries with dimensions  $50\ \mu\text{m}$  by  $1\ \text{mm}$ . In contrast to the tape or SU-8 channels, we anticipate the rectangular capillaries have the same chemistry and roughness on all channel surfaces. In contrast with the tape channels, the capillaries have no obvious local defects that may trigger the jet to form from a stress concentration. As a result of the homogenous and smooth surface of the glass capillaries, we observe that the jet always formed in the center (see Fig. 7). Slight variations in the jet position throughout the central region of the channel were evident, but we do not observe that the jet moves to the side of the channel as is the case with tape and some SU-8 channels.

We note that the observations discussed above are in channels with a height of  $50\ \mu\text{m}$  or less. Previous measurements of flow profiles without jetting of CPyCl/NaSal solutions [40] or other surfactant solutions were conducted in channels with a height of  $200\ \mu\text{m}$  and larger. This suggests that the absolute size of the channel might play a role in the formation of the jet, even though inertia is still negligible for these geometries. Results from flow stability analyses report that the channel height plays a role in the flow stability due to the relative size of the micelles to the channel dimension [29,32].

To see if the channel size has any influence on jetting, channels are constructed from  $350\ \mu\text{m}$  thick double-sided tape with a channel width of  $2.3\ \text{mm}$ . We observe similar jetting behavior in the larger channels as well, and the jet is also located near the tape side walls. Channel size will become relevant at larger length scales than investigated here, particularly when the Reynolds number ( $Re$ ) approaches unity and inertia becomes important. The flow in the  $350\ \mu\text{m}$  channel remains at negligible Reynolds number,  $Re \approx 10^{-5}$ . We conclude that channel size does not appear to significantly alter the jetting behavior over the range of channel heights we have investigated.

#### D. Channel aspect ratio

While we observe that the location of the jet and character of unstable flow depends on channel size, geometry, and wall roughness, the absence of observations in round capillaries suggest that channel aspect ratio is an important factor in the jetting behavior. Previous measurements of the same CPyCl/NaSal system in pressure-driven capillary flow demonstrated temporal oscillations in the local flow rate. Pressure-driven flow measurements of WLMs have used round capillaries [37], while only a limited number of groups have used rectangular cross-section geometries [35,44,55,56]. ‘‘Spurting’’ flow, which is characterized by a rapid jump in volumetric flow as pressure increases and often accompanied by temporal oscillations in the flow velocity, has been observed in round capillaries by a number of different groups [37,57].

For the round capillary or a square channel, there is no preferred cross-stream dimension for a spatially isolated high shear rate region. If volumetric flow is controlled in a round capillary, the stress across the capillary cross section adjusts in order to access shear rates that satisfy the volumetric flow constraint. While this is also possible for a 2D planar Poiseuille flow profile, our observations shown above demonstrate that the finite width channel results in jetting. The distribution of stress in the channel allows for stable and spatially distinct separation of wall shear rates, because a jet can form and self-constrict (as will be shown below with flow simulations) and therefore adjust to the applied volumetric flow.

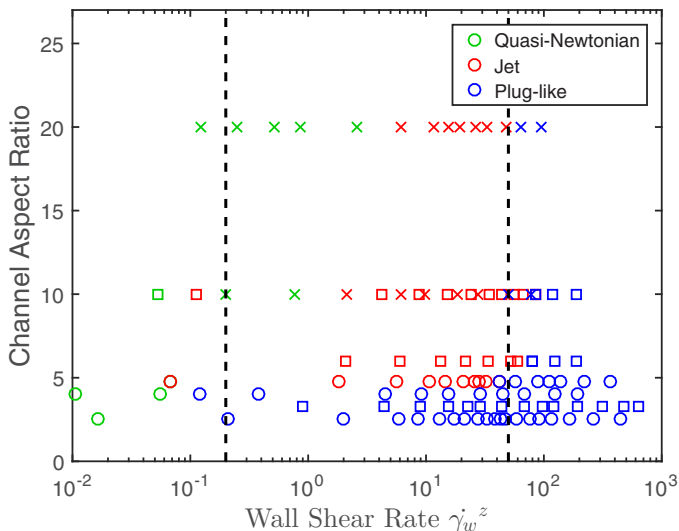


FIG. 8. Phase diagram for flow behavior as a function of aspect ratio and wall shear rate. Data are shown for channels constructed from 350  $\mu\text{m}$  thick tape (o), 100  $\mu\text{m}$  tape ( $\square$ ), and rectangular capillaries with  $h = 50 \mu\text{m}$  (x). As noted in the legend, quasi-Newtonian, jet and pluglike flow are represented by green, red, and blue colors respectively.

We investigated the effect of channel aspect ratio on flow behavior by constructing channels from different thickness tape, 100  $\mu\text{m}$  and 350  $\mu\text{m}$ , and then cutting channels of varying width to produce channels with aspect ratio in the range of 2–10. We also plot data from the rectangular capillary with AR = 10 and AR = 20, and SU-8 channels, AR = 10 (Fig. 8). We define the unstable flow as any flow that has a significant and persistent flow gradient across the channel width. The pluglike flow is characterized by a uniform flow across the channel width. We observe that the crossover between pluglike flow and jetting is around  $\text{AR} \cong 4\text{--}5$ . We note that the  $\text{AR} \cong 3\text{--}4$  show transient asymmetries in the flow immediately after the volumetric flow is adjusted. This transient behavior has been recently described by Kim *et al.* 2016 [58] for sodium lauryl ether 3 sulfate sodium lauryl sulfate system in a channel with AR = 5.

We note that the pluglike flow at low AR exhibits temporal velocity fluctuations with increasing frequency as flow is increased. We also observe velocity fluctuations in pluglike flow in high aspect ratio channels. The observation is consistent with previous measurements of flow through round capillaries above the threshold for pluglike flow [42,57].

Similar to the low concentration solution, the apparent or approximate shear rate across the channel width Eq. (6) becomes an important parameter in understanding the flow of shear thinning fluids in rectangular microfluidic channels. Aspect ratio adjusts the relative magnitude of the characteristic shear rates in the two principal cross stream directions. While the apparent shear rates in both the  $y$  and  $z$  directions will vary linearly with volumetric flow, the wall shear rate computed will vary nonlinearly with flow according to Eq. (2).

To show the relative magnitude of the two wall shear rates we plot the  $y$ -direction wall shear rate metric,  $\dot{\gamma}_w^y(Q)$ , as a function of the  $z$ -direction wall shear rate,  $\dot{\gamma}_w^z(Q)$ , for various aspect ratios (Fig. 9). We compare both wall shear rates to the critical shear rates,  $\dot{\gamma}_1$  and  $\dot{\gamma}_2$ . Intuitively, small aspect ratio channels have similar wall shear rates in the  $y$  and  $z$  directions, therefore the flow profile both directions will transition to a pluglike state at nearly the same volumetric flow. As the aspect ratio is increased, the difference in shear rates leads to a range of volumetric flow values where  $\dot{\gamma}_w^z > \dot{\gamma}_1$  and  $\dot{\gamma}_w^y < \dot{\gamma}_1$  and jetting occurs. While this analysis shows that jetting may occur for AR = 2 and AR = 4, other factors in experiments such as wall roughness will alter the stress field

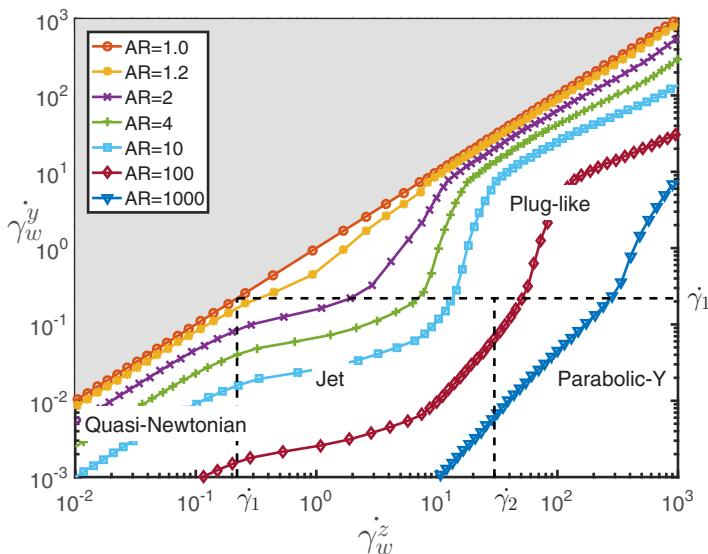


FIG. 9. Comparison of  $y$ - and  $z$ -direction wall shear rates for different aspect ratios as a function of volumetric flow. Wall shear rates calculated from Eq. (3) using the  $y$ - and  $z$ -direction average wall shear rates.

in the channel. We cannot therefore define a critical aspect ratio for jetting from this analysis, but it does show that volumetric flows where jetting is expected increases with aspect ratio.

An interesting situation arises at high aspect ratios ( $AR \gg 10$ ) where the average wall shear rate in the  $z$ -direction exceeds the upper critical value  $\dot{\gamma}_w^z > \dot{\gamma}_2$  and the  $y$ -direction wall shear rate remains less than the lower critical shear rate,  $\dot{\gamma}_w^y < \dot{\gamma}_1$ . In this situation, the entire top and bottom walls are in the upper shear rate branch while the side walls are still stable in the low shear rate branch. We distinguish this from jetting because there is a uniform shear rate in the upper shear rate branch along the top and bottom walls and categorize it as parabolic-Y. While we do not investigate channel aspect ratios greater than  $AR = 20$ , and thus do not access parabolic-Y experimentally, this analysis provides insight into the possible flow fields for shear banding fluids. We do show an example of the parabolic-Y flow profile across the channel width using simulations.

### E. Entrance effects

Entrance regions present a particular challenge for viscoelastic fluids in microfluidic channels. Stresses initiated at the entrance can lead to unusual downstream flow profiles [59–61]. We next examine the channel entrance region during the onset and development of jetting using PIV. Channels from SU-8 were made with either a hyperbolic or a  $45^\circ$  angle entrance. Two hyperbolic entrances constrict the flow from a width of 2 mm to  $200 \mu\text{m}$  in width; one channel has an entrance length of  $200 \mu\text{m}$  while the other of these has an entrance length of 2 mm. The  $45^\circ$  angle entrance tapers from 1 mm to  $200 \mu\text{m}$  width. All channels have a main channel section of  $20 \mu\text{m}$  height and  $200 \mu\text{m}$  width.

The hyperbolic entrance was chosen because it produces a constant extensional strain rate along the centerline of the channel [62]. The flow at steady state in the hyperbolic  $200 \mu\text{m}$  entrance length channel demonstrates the flow in the quasi-Newtonian and jetting (Fig. 10). In the quasi-Newtonian regime, the flow is fairly uniform across the channel width, but spatial variations in the flow are clearly present. This is consistent with the cross-stream profile shown in Fig. 6(a), which also showed slight deviations from a Newtonian flow. The presence of spatial variations and flow near the wall shows that even when all wall shear rates are below the critical value, a precursor to jetting may be present.

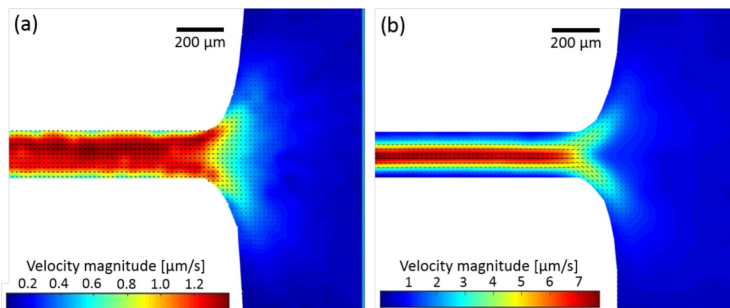


FIG. 10. The steady state flow field of the high concentration system measured with PIV at the entrance of a  $200\ \mu\text{m}$  channel showing (a) quasi-Newtonian flow and (b) jetting flow. (a) Quasi-Newtonian behavior is shown at steady state at a flow rate  $Q = 0.002\ \text{nl/s}$  and  $\dot{\gamma}_w^z = 0.18\ \text{s}^{-1}$  determined from Eq. (2). While the flow is mostly uniform across the channel, the flow fields shows some velocity variations, indicating that the wall shear rate is close to the critical shear rate,  $\dot{\gamma}_1$ . (b) Jetting behavior is shown at steady state at a flow rate  $Q = 0.017\ \text{nl/s}$  and  $\dot{\gamma}_w^z = 15.7\ \text{s}^{-1}$  determined from Eq. (2). At the channel entrance, two high-velocity regions along the sides of the entrance converge into one jet located in the center of the channel.

Figure 10(b) shows the jet forming near each of the channel entrance walls and merging into a single jet in the center of the channel [63]. This is the entrance for the SU-8 B channel discussed above. A symmetric contribution to the jet from both sides of the channel entrance indicates that there are similar stresses experienced by the fluid along each side of the channel entrance. The jet remains in the same position farther downstream; the cross-section measurements shown in Fig. 6 using this channel were performed about 500 mm downstream from the channel entrance.

In Fig. 11 we show the temporal development from an initially quiescent flow to a steady state in the pluglike flow regime. After 20 s, the flow field that develops is qualitatively similar to the jetting flow shown in Fig. 10(b), i.e., two high-velocity regions near the entrance sidewalls merging into a centrally located jet. This jet grows until it fills the entire channel as shown at  $t = 30\ \text{s}$ . The two jets that form along the sides of the channel entrance extend back into the upstream channel section. Subsequently, the two jets merge into one jet that, as a result of the larger width of the upstream section, is stable in the upstream section of the channel. We note that the development of a stable jet upstream of a hyperbolic entrance has been previously observed for a CPyCl/NaSal solution [63].

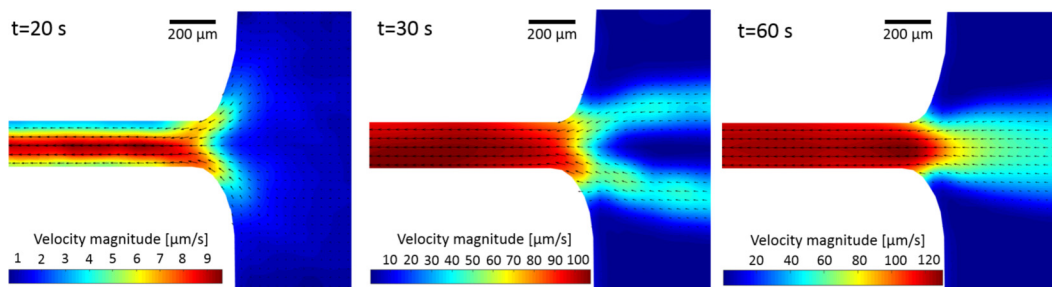


FIG. 11. A sequence of PIV images showing the temporal evolution of the flow field for the high concentration system at the entrance of a  $200\ \mu\text{m}$  channel in the pluglike regime. The flow reaches a steady state flow rate of  $Q = 0.44\ \text{nl/s}$  and  $\dot{\gamma}_w^z = 90.5\ \text{s}^{-1}$  determined from Eq. (2). At 20 s, two jets form along the sides of the entrance and merge to form a single jet in the main channel, similar to the behavior shown in Figure 10(b). At 30 s, uniform pluglike flow develops in the main channel and the two jets along the sides of the entrance extend upstream. At  $t = 60\ \text{s}$ , the flow reaches a steady state, the two jets have merged into a single stable jet upstream of the entrance.

The evolution of jet formation is influenced by normal forces, which is discussed in a later section on flow simulations.

The two other entrance geometries tested show similar transitions from quasi-Newtonian to jetting and finally to pluglike flow. The main difference between different channels was where the jet initiated. The 45 degree and 2 mm hyperbolic channels showed a jet forming on only one side of the channel, which we attribute to slight defects in the channel construction that may be caused by misalignment of SU-8 layers and produce a perturbation to the stress along one side of the channel. The first region of the channel that reaches a stress value with a multivalued shear rate will be able to jump to a high shear rate, and as a result the jet will always form on that side. A slight velocity increase is still present on the nonjetting side of the channel entrance, although this high-velocity region does not persist downstream and dissipates just past the entrance.

The 45° channel entrance shows the jet forming at one corner of the entrance and then extending into the 1 mm wide upstream channel [63]. The narrower upstream section of the channel allows both main and upstream channel sections to stabilize in the jetting regime. The evolution of the jet originates at the point of highest stress, which in this case is at the entrance corner. We note that this jet extends backwards upstream until reaching the entrance port of the channel not shown in the video.

All of the channel entrances discussed above constrict the flow by narrowing the channel width. As a result, a nonuniform stress field develops across the channel entrance, indicated by the jets that form along the sides of the entrance. We constructed a channel from glass and double-sided tape that reduces from a square cross section, of approximately 2 mm width and 2 mm height, to a main section of 100  $\mu\text{m}$  height and 2 mm width. A reduction in the channel height produces a more uniform stress and flow field across the channel entrance. While this reduces any directional preference for the jet to form, it still forms although about 1 cm from the entrance. In this case, roughness in the edges of the tape likely cause perturbations to the stress that preference the flow to one side of the channel. This shows that even for a channel with an entrance designed to have symmetric flow, the flow will still separate into a stable jet.

We conclude that the channel entrance does not have a significant effect on the presence of the jets in general. Rather, the entrance geometry can alter the location of the jet in the channel by creating a localized stress that initiates the wall shear rate to jump into the higher shear rate.

#### IV. SIMULATIONS

The experimental results suggest that a shear banding fluid will transition to the banded flow behavior in high aspect ratio rectangular channels. In all cases, the volumetric flow constraint can be satisfied by a velocity profile composed of stable shear rates (see schematic Fig. 2), even when the parameter  $\dot{\gamma}_w^z$  is an unstable shear rate. The flow field can adjust by altering the position of the shear band, the kink in the velocity profile as shown in the schematic Fig. 2(c). As a result, the flow constraint can be satisfied by a velocity profile composed of the stable shear rates and a velocity profile with a kink is produced [56]. This has been shown for different constitutive models with nonmonotonic stress curve, including Giesekus and VCM [30,64]. Two-dimensional simulations and experiments have shown, however, that the shear banded velocity profiles can become unstable and exhibit undulations in the interface between high and low shear rates [21,29,65,66]. Our experiments and those of Haward *et al.* suggest that these undulations may destabilize the uniform banded flow in rectangular channels so that a jet may form. We use the Johnson-Segalman (JS) model to explore jetting and the conditions that promote or suppress jet formation [67].

The JS model is chosen as a model fluid because of its relative simplicity and the ability to represent shear banding fluids due to its nonmonotonic constitutive equation [68,69]. We implement the JS model in a finite volume code developed to model viscoelastic simulations using OpenFOAM, an open-source computational fluids solver. A number of different viscoelastic models have already been used in OpenFOAM and compared with experimental results from the literature [70]. The model solves incompressible flows of viscoelastic fluids satisfying the continuity equation and the

TABLE III. Parameters for the Johnson-Segalman model.

Parameter	Value
$\eta_s$	0.5 [Pa-s]
$\eta_m$	120 [Pa-s]
$\lambda$	4 [s]
$\xi$	1

momentum equation:

$$\nabla \cdot \mathbf{u} = 0, \quad \rho \frac{D\mathbf{u}}{Dt} = \nabla \cdot (\mathbf{T} + 2\eta_s \mathbf{D} - p\mathbf{I}), \quad (7)$$

where the quantity in parentheses is the total stress and  $\mathbf{T}$  is the micellar stress determined by the JS constitutive model,  $p$  is pressure,  $\eta_s$  is the solvent viscosity, and  $\mathbf{D}$  is the rate-of-deformation tensor. The micelle stress here satisfies the JS constitutive model:

$$\mathbf{T} + \lambda \left[ \left( 1 - \frac{\xi}{2} \right) \overset{\nabla}{\mathbf{T}} + \frac{\xi}{2} \overset{\Delta}{\mathbf{T}} \right] = 2\eta_m \mathbf{D}, \quad (8)$$

where  $\overset{\nabla}{\mathbf{T}}$  and  $\overset{\Delta}{\mathbf{T}}$  denote the upper and lower convective derivatives respectively,  $\eta_m$  is the micellar viscosity, and  $\lambda$  is the relaxation time. The parameter,  $\xi$ , is a dimensionless parameter that controls the relative magnitude of the two convective derivatives. This parameter controls shear banding by introducing nonaffine motion to the shear components via the lower convective derivative. This model simplifies to the Oldroyd-B model when  $\xi = 0$ , which describes the dynamics of Hookean dumbbells. In this context, the nonaffine deformations introduce slip between the dumbbells. Although this model is phenomenological, the relative simplicity makes it amenable to studying shear banding behavior, even though it does not capture all the complexities, such as concentration gradients, of more detailed models. We therefore do not expect the model to quantitatively match our experimental results, but it is nevertheless instructive for understanding the relation between stress and flow in the microchannel that results in jetting.

The parameters for the JS model, shown in Table III, are chosen to produce a top jumping path along the shear stress curve that roughly matches the values measured from steady shear rheology for the high concentration system (Fig. 12). The choice of JS parameters provides quantitatively similar values compared to the zero shear rate viscosity,  $\eta_0$ , lower critical shear rate,  $\dot{\gamma}_1$ , and relaxation time,  $\lambda$ , of the high concentration system from Tables I and II. The JS model does not fit the steady shear rheology data at high shear rates. This is because the JS model is Newtonian in the high shear rate, while the WLM solutions are shear thinning at high shear rates. Importantly, the JS model does produce a nonmonotonic stress curve with a well-defined range of unstable shear rates, in this case approximately  $(0.12 - 4) \text{ s}^{-1}$ . The lower and upper shear rate limits, denoted  $\dot{\gamma}_L$  and  $\dot{\gamma}_U$ , respectively, define the range unstable for the JS model. We note that for the parameters chosen, the shear stress at the lower critical shear rate is approximately 4 times higher than the stress at the high critical shear rate. This difference in stress magnitude will be relevant for the distribution of stress in the channel.

The 3D rectangular domain for simulations has a cross-section dimension of  $20 \mu\text{m} \times 200 \mu\text{m}$  (to match the SU-8 channel) and a length of  $800 \mu\text{m}$ . A flow-controlled experimental system is replicated by setting the channel inlet at a fixed integrated velocity, which is adjusted to change the volumetric flow. The outlet boundary condition is set at a constant pressure, and the normal direction gradient (along  $x$ ) of the velocity and polymer stress are set at zero. The fluid velocity is set at zero (no slip) at the top, bottom, and side walls of the channel. The gradient normal to the wall surfaces for the other variables, pressure and micelle stress, are set as zero. The flow is initialized by running

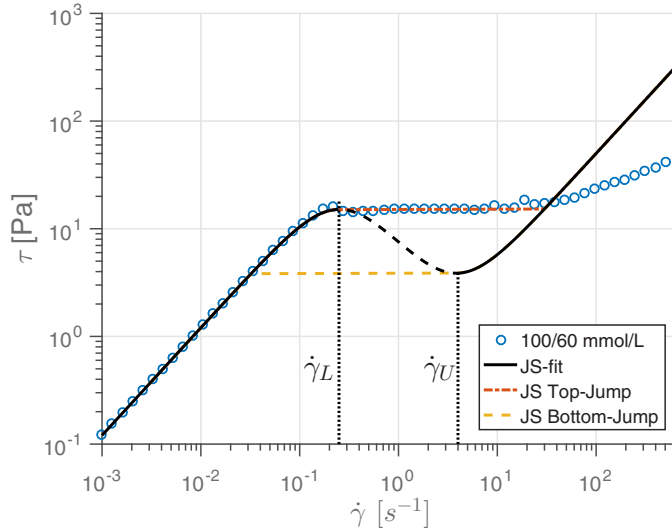


FIG. 12. Shear stress curve for the JS model (assuming simple shear for comparison with data replotted from Fig. 4) using the parameters shown in Table III compared to steady shear measurements for the high concentration system. Transitions by top jumping and bottom jumping for the JS are also shown in dash-dot and dashed lines respectively. The parameters of the JS model are set to match a top jumping path with the high concentration rheology. The unstable shear rates are shown between the two critical shear rates,  $\dot{\gamma}_L$  and  $\dot{\gamma}_U$ .

the simulation at a weak flow,  $U_{\text{avg}} = 0.1 \mu\text{m/s}$ , and all simulation runs with volumetric flows are started from this initial flow field.

At low volumetric flows, the flow profile matches a Newtonian-like flow [Fig. 13(a)], which is to be expected from the JS model for weaker stresses on the linear portion of the stress curve. As volumetric flow increases, a jetting flow is observed similar to the behavior seen in experiments.

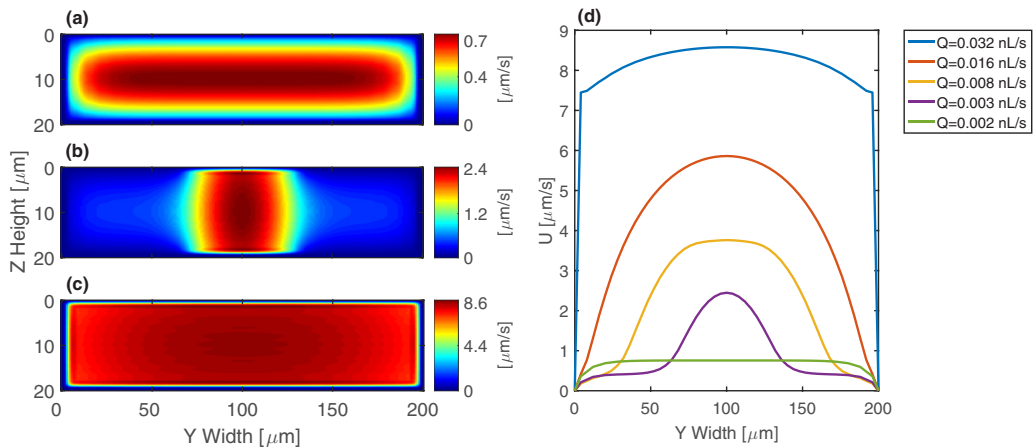


FIG. 13. Cross section velocity profiles from simulation of a JS viscoelastic fluid in a rectangular channel. (a) Quasi-Newtonian flow field at  $Q = 0.002 \text{ nL/s}$ . (b) Jetting flow at  $Q = 0.003 \text{ nL/s}$ . (c) Pluglike flow at  $Q = 0.032 \text{ nL/s}$ . The effective channel width determined from the uniform plug flow for the same volumetric flow is  $199.7 \mu\text{m}$ . (d) Velocity profile across the channel width for the  $\text{AR} = 10$  channel at various volumetric flows. The flow transitions from quasi-Newtonian to jetting to pluglike.

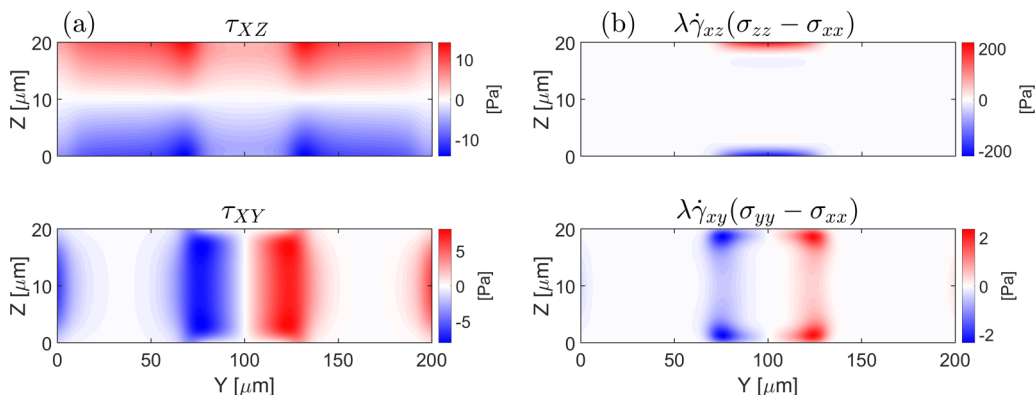


FIG. 14. Cross section profiles for (a) shear stresses and (b) the normal stress terms from numerical simulation of JS model for jetting flow at steady state.

This transition occurs when the  $z$ -direction wall shear stress exceeds the critical value,  $\dot{\gamma}_L$ , defined from the JS model (Fig. 12). The flow profile in the  $z$ -direction across the jet is pluglike, noticeable in Fig. 13(b). A large velocity gradient borders the high-velocity profile on the top and bottom walls, corresponding to the high shear rate part of the stress curve. As volumetric flow is increased, the top and bottom wall regions with a high shear rate fill an increasing portion until the entire channel is filled and we observe pluglike flow; see Fig. 13(c).

To better demonstrate transitions from quasi-Newtonian, jetting, and pluglike flows, we plot the velocity profile across the channel width in Fig. 13(d). The transition from quasi-Newtonian to jetting is apparent when a narrow parabolic profile forms in the center of the channel. For the jetting flow, the maximum velocity outside of the jet region at  $Q = 0.003$  nl/s is in fact lower than the maximum velocity of the quasi-Newtonian flow at  $Q = 0.002$  nl/s. The transition to jetting results in greater flow within the jet and a weaker flow outside the jet. Figure 13(d) shows that as volumetric flow increases, both the width of the jetting region and the maximum velocity in the jet increase. The velocity gradient on the sides of the jetting flow however remain similar while volumetric flow increases. This is a result of a similar composition of stresses surrounding the jet, which shift towards the sidewalls as flow increases but do not change significantly in magnitude.

At  $Q = 0.016$  nl/s, the  $y$ -direction flow profile is close to parabolic. This exemplifies the situation where the entire top and bottom walls are in the high shear rate branch but the side walls remain stable in the low shear rate branch. In context of the directional wall shear rate discussed in the aspect ratio section, the average wall shear rate is above the upper critical shear rate,  $\dot{\gamma}_w^z > \dot{\gamma}_U$ , but the wall shear rate along the side remains below the first critical shear rate  $\dot{\gamma}_w^y < \dot{\gamma}_L$ . The transition from parabolic-Y flow to pluglike flow occurs only when  $\dot{\gamma}_w^y > \dot{\gamma}_L$ , which is shown in Fig. 13(d) at  $Q = 0.032$  nl/s.

An analysis of the micellar stress field is needed for a better understanding of the jetting flow. The  $\tau_{xz}$  and  $\tau_{xy}$  shear stresses are shown in the channel cross section in Fig. 14(a). As expected for flows in a rectangular channel,  $\tau_{xz}$  is the largest shear stress component because it spans the shortest channel dimension,  $h$ . A large variation in the  $\tau_{xz}$  magnitude is also apparent across the jetting region, with relatively weak  $\tau_{xz}$  stresses located in the jetting region, coincident with the largest shear rates. We note that  $\tau_{xz}$  remains linear across the  $z$  direction, even as it varies in magnitude in the  $y$  direction. This variation in wall stress can be understood in context of the JS shear stress curve (Fig. 12), whose shear stress at the upper critical shear rate,  $\dot{\gamma}_U$ , is approximately 4 times lower than at the lower critical shear rate,  $\dot{\gamma}_L$ . Rather than following the top-jumping path shown in Fig. 12, the wall shear rate inside the jet jumps to the high shear rate branch, at a lower stress. This is similar to the decrease in shear stress as a function of shear rate observed in shear-rate-controlled rheometry

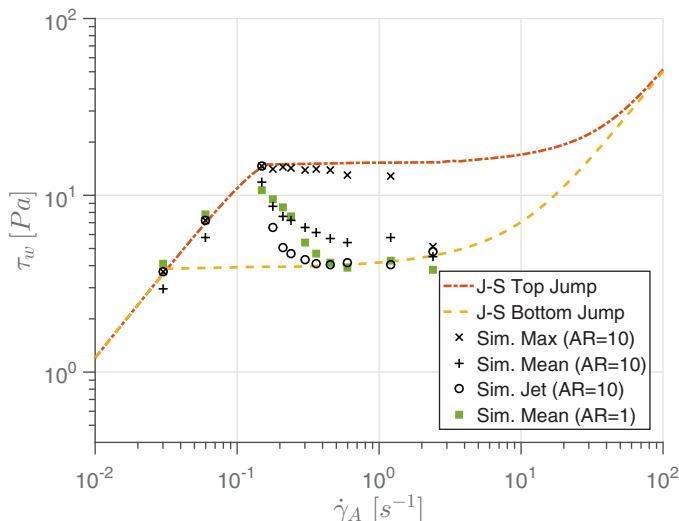


FIG. 15. Plot of wall shear stress as a function of apparent shear rate (1) from the JS model simulations. The shear stress at the wall is compared for the jet region (o), the maximum value (x), and the mean over entire cross section perimeter (+) for aspect ratio 10. The mean is also shown for aspect ratio 1. The data from simulations are compared to wall shear stress predicted from the Weissenberg-Rabinowitsch-Mooney analysis for top jumping (dash-dot) and bottom jumping (dashed) curves from the JS model.

for the high concentration system [71]. In the jetting flow, however, the high and low shear rates coexist along the top and bottom walls at different shear stress.

In the JS model, normal stresses contribute to the shear stress balance as a term that includes the normal stress difference [67,68]. For example, when  $\xi = 1$  the  $x$ - $z$  stress balance includes the normal stress difference term,  $\lambda \dot{\gamma}_{xz}(\sigma_{zz} - \sigma_{xx})$ , where  $\sigma$  denotes normal stress. We plot the normal stress difference terms that contribute to the  $x$ - $y$  and  $x$ - $z$  stress balance to exemplify the contribution of normal stresses [Fig. 14(b)]. The normal stress difference term for the  $x$ - $y$  stress balance is largest in the high shear rate region near the wall bordering the jet. The magnitude of the normal stress difference term is also large compared to the  $\tau_{xz}$  shear stress in the same location. This term compensates for the decrease in the  $\tau_{xz}$  shear stress in the negative slope portion of the stress curve and balances the velocity gradient. As the jet begins to form in time, the normal stress term magnitude increases and the region of high stress shrinks as the jet narrows.

The focusing of flow into a narrow jet is driven and sustained by the stress balance in the  $y$  direction. This is exemplified by the  $x$ - $y$  stress balance. At steady state, the  $\tau_{xy}$  shear stresses surround the jet where the velocity gradients are greatest. The magnitude of the normal stress term in the  $x$ - $y$  stress balance,  $\lambda \dot{\gamma}_{xy}(\sigma_{yy} - \sigma_{xx})$ , is greatest in the region surrounding the jet as well. While this normal stress term is not as large as the  $x$ - $z$  component, it nevertheless contributes to the  $x$ - $y$  stress balance surrounding the jet. As the jetting flow develops, the  $x$ - $y$  shear stress and normal stress difference terms grow in magnitude beginning from the edges of the channel. The imbalance of stresses in the  $y$  direction at the edges lead to the flow focusing into a jet. The balance of stresses in the  $y$  direction leads to a stable jet. As volumetric flow is increased and the width of the jet increases, the cross-section stress profiles remain at a similar in magnitude but the stresses surrounding the jet spread until they are confined by the side walls.

We show the development of wall shear stresses,  $\tau_w$ , as a function of flow by plotting the maximum wall shear stress and the wall shear stress adjacent to the jet as a function of apparent shear rate (Fig. 15). We compare these data to the expected wall shear stress for a top and bottom jumping JS model from the Weissenberg-Rabinowitsch-Mooney analysis (Eq. 2). The transition to jetting flow corresponds to the sharp change in the top jumping curve at approximately  $\dot{\gamma}_L = 0.15 \text{ s}^{-1}$ . Flows

below this value produce a Newtonian flow profile, and the maximum wall stress occurs uniformly across the top and bottom surfaces. These wall stresses match well with the top jumping curve. Once jetting occurs, the shear stress in the jet region rapidly decreases and follows the bottom jumping curve while the maximum stress remains near the top jumping curve. The mean shear stress along the channel walls remains between the top and bottom jumping curves, but decreases in magnitude as the size of the jet increases and more wall surface is at the lower stress value. Once the entire channel transitions to pluglike flow [Fig. 13(c)], the maximum and mean value are equal, and both are on the bottom jumping curve.

We also compare the mean wall shear stress in the rectangular channel,  $AR = 10$ , to the mean wall shear stress in a square channel,  $AR = 1$ . The latter does not exhibit jetting behavior, but the onset of shear banding and accompanying decrease in wall stress occur at the same apparent shear rate. For both aspect ratios, the wall shear stress does not immediately decrease to the bottom jumping curve because the wall shear stress is mixed between the top and bottom jumping curves. This transition is broadened further when the  $AR$  is sufficiently large for jetting. The similar wall stress behavior observed in rectangular capillaries of  $AR = 1$  and  $AR = 10$  suggests that rectangular capillaries can produce qualitatively different behavior than circular capillaries. Circular capillaries cannot have steady wall shear stress that is mixed between the two branches.

Our results demonstrate that the JS model qualitatively replicates the jetting behavior seen in experiments and that normal stress is important for the development of the jetting. Additionally, the model shows the transitions from quasi-Newtonian, jetting, and pluglike flow as volumetric flow is increased. The results show that normal stresses triggered by the high shear rate at the walls are required to balance the shear stresses associated with the jetting flow field. We expect other constitutive models that produce a nonmonotonic stress curve will produce similar stress fields and are likely to display similar jetting behavior. Furthermore, we suspect that jetting does not explicitly require shear banding. Strongly shear thinning fluids that exhibit substantial normal stress differences might also exhibit jetting in rectangular channels, through a similar stress field.

## V. CONCLUSION

In this paper, we investigate the jetting behavior of a shear banding fluid in high aspect ratio rectangular channels. The jet forms over a finite volumetric flow range, below which we observe quasi-Newtonian flow, and at higher flows we observe pluglike flow. The jetting flow occurs in different channel geometries and channels constructed from various wall materials. If the channel wall is made from a rough material, such as the rough edge of cut double-sided tape, the jet is likely to form near the rough surface. Smooth and uniform surfaces, such as a rectangular glass capillary, lead to the jet forming in the middle of the channel. We conclude that the jet forms in regions of higher stress. This is further supported by observing the development of the jet in various channel entrances where stress concentrations form near the corner of the entrance. Jetting is observed over a range of  $z$ -direction wall shear rates that correspond to the plateau region of the shear stress curve characteristic of shear banding fluids, indicating that the jetting behavior here is associated with the onset of shear banding.

The JS viscoelastic model is used in 3D numerical simulations to model the behavior of a shear banding fluid in a rectangular channel. Results from the simulations show the same transition from quasi-Newtonian behavior to jetting and finally pluglike flow that we observe in experiments. Stress profiles from the simulations show that shear banding leads to high shear rates along the wall and large positive normal stresses in the flow direction. Negative normal stresses develop in these same locations and balance the velocity gradients bordering the high-velocity jet. We also compare the wall shear stresses in the channel to predictions from the WRM analysis for the JS model. The walls within the jet follow a bottom jumping path of the stress curve and lead to a lower wall shear stress while the walls outside the jet remain at a higher stress.

We believe our results are similar to the jetting instability observed by Haward *et al.* [44] using CTAB/NaSal WLMs. The main difference in that system is that the linear rheology for their WLM

system did not exhibit a stress plateau indicative of shear banding behavior. We did not observe the jetting behavior at a lower concentration of the CPyCl/NaSal system, but we did observe that velocity gradients extended further across the channel width. There are examples of shear banding like behavior for entangled polymers with monotonic stress curve [64,72–75]. It is also possible that the large differences in shear rates that a nonlinear, yet monotonic, stress curve could lead to jetting-like behavior [76].

We note that other similar experiments of shear banding fluids in rectangular microfluidic channels did not report this behavior. It is possible that for intermediate channel aspect ratios ( $AR \approx 5-8$ ), the shear rate range for the unstable behavior was not sampled. Our results add to evidence that the flow of non-Newtonian fluids rectangular microfluidic channels is indeed complex, in particular that gradients across the channel width are not always negligible. This complex behavior also presents opportunities for manipulation of flows in microfluidic channels, for instance, as a sorting mechanism or as a means of producing flow through stress localizations.

## VI. DISCLAIMER

Certain commercial materials and equipment are identified in this paper in order to adequately specify the experimental procedure. In no case does such identification imply recommendation or endorsement by the National Institute of Standards and Technology, nor does it imply that these are necessarily the best available for the purpose.

Official contribution of the National Institute of Standards and Technology; not subject to copyright in the United States.

## ACKNOWLEDGMENTS

We acknowledge funding from NIST on a Chip. We thank Kathleen Weigandt for assistance with rheology measurements and Javen Weston and Peter Olmsted for helpful discussions.

- 
- [1] W. A. Wakeham, A. Nagashima, and J. Sengers, *Measurement of the Transport Properties of Fluids*, Vol. 3 (Blackwell Science Publications, Oxford, 1991).
  - [2] K. Weissenberg, On the viscosity of elasticity of brines, *Zeitschrift Phys. Chem. Abteilung A Chem. Thermodyn. Kin. Elektrochem. Eigenschaftslehre* **145**, 1 (1929).
  - [3] S. D. Hudson, P. Sarangapani, J. A. Pathak, and K. B. Migler, A microliter capillary rheometer for characterization of protein solutions, *J.Pharmaceut. Sci.* **104**, 678 (2015).
  - [4] C. J. Pipe, T. S. Majmudar, and G. H. McKinley, High shear rate viscometry, *Rheol. Acta* **47**, 621 (2008).
  - [5] V. L. Dharmaraj, P. D. Godfrin, Y. Liu, and S. D. Hudson, Rheology of clustering protein solutions, *Biomicrofluidics* **10**, 043509 (2016).
  - [6] R. G. Larson, *The Structure and Rheology of Complex Fluids* (Oxford University Press, New York, 1999).
  - [7] M. Cates, Nonlinear viscoelasticity of wormlike micelles (and other reversibly breakable polymers), *J. Phys. Chem.* **94**, 371 (1990).
  - [8] C. A. Dreiss, Wormlike micelles: Where do we stand? Recent developments, linear rheology and scattering techniques, *Soft Matter* **3**, 956 (2007).
  - [9] E. Cappelaere, J. Berret, J. Decruppe, R. Cressely, and P. Lindner, Rheology, birefringence, and small-angle neutron scattering in a charged micellar system: Evidence of a shear-induced phase transition, *Phys. Rev. E* **56**, 1869 (1997).
  - [10] O. Manero, F. Bautista, J. Soltero, and J. Puig, Dynamics of worm-like micelles: The Cox–Merz rule, *J. Non-Newtonian Fluid Mech.* **106**, 1 (2002).
  - [11] M. E. Cates and S. M. Fielding, Rheology of giant micelles, *Adv. Phys.* **55**, 799 (2006).

- [12] W. Zou and R. G. Larson, A mesoscopic simulation method for predicting the rheology of semi-dilute wormlike micellar solutions, *J. Rheol.* (1978–present) **58**, 681 (2014).
- [13] W. Zou, X. Tang, M. Weaver, P. Koenig, and R. G. Larson, Determination of characteristic lengths and times for wormlike micelle solutions from rheology using a mesoscopic simulation method, *J. Rheol.* (1978–present) **59**, 903 (2015).
- [14] G. Ovarlez, S. Rodts, X. Chateau, and P. Coussot, Phenomenology and physical origin of shear localization and shear banding in complex fluids, *Rheol. Acta* **48**, 831 (2009).
- [15] S. M. Fielding, Complex dynamics of shear banded flows, *Soft Matter* **3**, 1262 (2007).
- [16] P. D. Olmsted, Perspectives on shear banding in complex fluids, *Rheol. Acta* **47**, 283 (2008).
- [17] F. Bautista, J. Soltero, J. Pérez-López, J. Puig, and O. Manero, On the shear banding flow of elongated micellar solutions, *J. Non-Newtonian Fluid Mech.* **94**, 57 (2000).
- [18] J. Ballesta and S. Manneville, The Faraday instability in wormlike micelle solutions, *J. Non-Newtonian Fluid Mech.* **147**, 23 (2007).
- [19] T. Divoux, M. A. Fardin, S. Manneville, and S. Lerouge, Shear banding of complex fluids, *Annu. Rev. Fluid Mech.* **48**, 81 (2016).
- [20] J.-B. Salmon, A. Colin, S. Manneville, and F. Molino, Velocity Profiles in Shear-Banding Wormlike Micelles, *Phys. Rev. Lett.* **90**, 228303 (2003).
- [21] P. Nghe, S. Fielding, P. Tabeling, and A. Ajdari, Interfacially Driven Instability in the Microchannel Flow of a Shear-Banding Fluid, *Phys. Rev. Lett.* **104**, 248303 (2010).
- [22] S. Lerouge, M. Argentina, and J.-P. Decruppe, Interface Instability in Shear-Banding Flow, *Phys. Rev. Lett.* **96**, 088301 (2006).
- [23] L. Bécu, S. Manneville, and A. Colin, Spatiotemporal Dynamics of Wormlike Micelles Under Shear, *Phys. Rev. Lett.* **93**, 018301 (2004).
- [24] M.-A. Fardin and S. Lerouge, Instabilities in wormlike micelle systems, *Eur. Phys. J. E* **35**, 1 (2012).
- [25] M. Fardin, T. Divoux, M. Guedeau-Boudeville, I. Buchet-Maulien, J. Browaeys, G. McKinley, S. Manneville, and S. Lerouge, Shear-banding in surfactant wormlike micelles: Elastic instabilities and wall slip, *Soft Matter* **8**, 2535 (2012).
- [26] K. W. Feindel and P. T. Callaghan, Anomalous shear banding: Multidimensional dynamics under fluctuating slip conditions, *Rheol. Acta* **49**, 1003 (2010).
- [27] A. F. Méndez-Sánchez, J. Pérez-González, L. De Vargas, J. R. Castrejón-Pita, A. A. Castrejón-Pita, and G. Huelsz, Particle image velocimetry of the unstable capillary flow of a micellar solution, *J. Rheol.* (1978–present) **47**, 1455 (2003).
- [28] S. Manneville, A. Colin, G. Watson, and F. Schosseler, Wall slip, shear banding, and instability in the flow of a triblock copolymer micellar solution, *Phys. Rev. E* **75**, 061502 (2007).
- [29] S. M. Fielding and H. J. Wilson, Shear banding and interfacial instability in planar Poiseuille flow, *J. Non-Newtonian Fluid Mech.* **165**, 196 (2010).
- [30] M. Cromer, L. P. Cook, and G. H. McKinley, Interfacial instability of pressure-driven channel flow for a two-species model of entangled wormlike micellar solutions, *J. Non-Newtonian Fluid Mech.* **166**, 566 (2011).
- [31] J. K. Dhont and W. J. Briels, Gradient and vorticity banding, *Rheol. Acta* **47**, 257 (2008).
- [32] S. M. Fielding, Vorticity structuring and velocity rolls triggered by gradient shear bands, *Phys. Rev. E* **76**, 016311 (2007).
- [33] C. R. López-Barrón, A. K. Gurnon, A. P. Eberle, L. Porcar, and N. J. Wagner, Microstructural evolution of a model, shear-banding micellar solution during shear startup and cessation, *Phys. Rev. E* **89**, 042301 (2014).
- [34] R. L. Moorcroft and S. M. Fielding, Shear banding in time-dependent flows of polymers and wormlike micelles, *J. Rheol.* (1978–present) **58**, 103 (2014).
- [35] C. Masselon, J.-B. Salmon, and A. Colin, Nonlocal Effects in Flows of Wormlike Micellar Solutions, *Phys. Rev. Lett.* **100**, 038301 (2008).
- [36] C. Masselon, A. Colin, and P. D. Olmsted, Influence of boundary conditions and confinement on nonlocal effects in flows of wormlike micellar systems, *Phys. Rev. E* **81**, 021502 (2010).
- [37] P. Callaghan, M. Cates, C. Rofe, and J. Smeulders, A study of the “Spurt Effect,” *J. Phys. II* **6**, 375 (1996).

- [38] R. Mair and P. Callaghan, Shear flow of wormlike micelles in pipe and cylindrical Couette geometries as studied by nuclear magnetic resonance microscopy, *J. Rheol.* (1978–present) **41**, 901 (1997).
- [39] M. Britton and P. Callaghan, Shear banding instability in wormlike micellar solutions, *Eur. Phys. J. B* **7**, 237 (1999).
- [40] T. J. Ober, J. Soulages, and G. H. McKinley, Spatially resolved quantitative rheo-optics of complex fluids in a microfluidic device, *J. Rheol.* (1978–present) **55**, 1127 (2011).
- [41] B. M. Marín-Santibáñez, J. Pérez-González, L. De Vargas, F. Rodríguez-González, and G. Huelasz, Rheometry-PIV of shear-thickening wormlike micelles, *Langmuir* **22**, 4015 (2006).
- [42] S. Hernández-Acosta, A. González-Alvarez, O. Manero, A. F. M. Sánchez, J. Pérez-González, and L. De Vargas, Capillary rheometry of micellar aqueous solutions, *J. Non-Newtonian Fluid Mech.* **85**, 229 (1999).
- [43] S. J. Haward, T. J. Ober, M. S. Oliveira, M. A. Alves, and G. H. McKinley, Extensional rheology and elastic instabilities of a wormlike micellar solution in a microfluidic cross-slot device, *Soft Matter* **8**, 536 (2012).
- [44] S. Haward, F. Galindo-Rosales, P. Ballesta, and M. Alves, Spatiotemporal flow instabilities of wormlike micellar solutions in rectangular microchannels, *Appl. Phys. Lett.* **104**, 124101 (2014).
- [45] See Supplemental Material at <http://link.aps.org/supplemental/10.1103/PhysRevFluids.2.033302> for videos show jetting and pluglike flow at the entrance of a  $200\ \mu\text{m}$  by  $20\ \mu\text{m}$  cross section channel. The pressure drop for each component in the flow system is estimated as a function of flow rate.
- [46] F. C. Cheong, B. J. Krishnatreya, and D. G. Grier, Strategies for three-dimensional particle tracking with holographic video microscopy, *Opt. Express* **18**, 13563 (2010).
- [47] N. T. Ouellette, H. Xu, and E. Bodenschatz, A quantitative study of three-dimensional Lagrangian particle tracking algorithms, *Exp. Fluids* **40**, 301 (2006).
- [48] W. Thielicke, The flapping flight of birds: Analysis and application, Ph.D. thesis, University of Groningen, 2014.
- [49] W. Thielicke and E. J. Stamhuis, PIVlab—Towards User-friendly, Affordable and Accurate Digital Particle Image Velocimetry in MATLAB, *J. Open Res. Softw.* **2**, e30 (2014).
- [50] M. Cates, Flow behaviour of entangled surfactant micelles, *J. Phys. Condens. Matter* **8**, 9167 (1996).
- [51] J. F. Berret, J. Appell, and G. Porte, Linear rheology of entangled wormlike micelles, *Langmuir* **9**, 2851 (1993).
- [52] E. Cappelaere and R. Cressely, Shear banding structure in viscoelastic micellar solutions, *Colloid Polymer Sci.* **275**, 407 (1997).
- [53] P. Fischer, E. K. Wheeler, and G. G. Fuller, Shear-banding structure orientated in the vorticity direction observed for equimolar micellar solution, *Rheol. Acta* **41**, 35 (2002).
- [54] M. P. Lettinga and S. Manneville, Competition Between Shear Banding and Wall Slip in Wormlike Micelles, *Phys. Rev. Lett.* **103**, 248302 (2009).
- [55] Y. Zhao, P. Cheung, and A. Q. Shen, Microfluidic flows of wormlike micellar solutions, *Adv. Colloid Interf. Sci.* **211**, 34 (2014).
- [56] M. Cromer, L. P. Cook, and G. H. McKinley, Pressure-driven flow of wormlike micellar solutions in rectilinear microchannels, *J. Non-Newtonian Fluid Mech.* **166**, 180 (2011).
- [57] W. Holmes, M. Lopez-Gonzalez, and P. Callaghan, Fluctuations in shear-banded flow seen by NMR velocimetry, *Europhys. Lett.* **64**, 274 (2003).
- [58] Y. Kim, A. Adams, W. H. Hartt, R. G. Larson, and M. J. Solomon, Transient, near-wall shear-band dynamics in channel flow of wormlike micelle solutions, *J. Non-Newtonian Fluid Mech.* **232**, 77 (2016).
- [59] R. J. Poole and M. A. Alves, Velocity overshoots in gradual contraction flows, *J. Non-Newtonian Fluid Mech.* **160**, 47 (2009).
- [60] R. J. Poole, M. P. Escudier, and P. J. Oliveira, Laminar flow of a viscoelastic shear-thinning liquid through a plane sudden expansion preceded by a gradual contraction, in *Proceedings of the Royal Society of London A: Mathematical, Physical and Engineering Sciences* (The Royal Society, 2005), Vol. 461, pp. 3827–3845.
- [61] H. T. Jahromi, M. Webster, J. Aguayo, and O. Manero, Numerical investigation of transient contraction flows for worm-like micellar systems using Bautista–Manero models, *J. Non-Newtonian Fluid Mech.* **166**, 102 (2011).

- [62] M. S. N. Oliveira, M. A. Alves, F. T. Pinho, and G. H. McKinley, Viscous flow through microfabricated hyperbolic contractions, [Exp. Fluids](#) **43**, 437 (2007).
- [63] T. J. Ober, S. J. Haward, C. J. Pipe, J. Soulages, and G. H. McKinley, Microfluidic extensional rheometry using a hyperbolic contraction geometry, [Rheol. Acta](#) **52**, 529 (2013).
- [64] M. Cromer, M. C. Villet, G. H. Fredrickson, and L. G. Leal, Shear banding in polymer solutions, [Phys. Fluids \(1994–present\)](#) **25**, 051703 (2013).
- [65] S. M. Fielding, Viscoelastic Taylor-Couette Instability of Shear Banded Flow, [Phys. Rev. Lett.](#) **104**, 198303 (2010).
- [66] M.-A. Fardin, T. Ober, C. Gay, G. Grégoire, G. McKinley, and S. Lerouge, Potential “ways of thinking” about the shear-banding phenomenon, [Soft Matter](#) **8**, 910 (2012).
- [67] M. Johnson and D. Segalman, A model for viscoelastic fluid behavior which allows non-affine deformation, [J. Non-Newtonian Fluid Mech.](#) **2**, 255 (1977).
- [68] G. C. Georgiou and D. Vlassopoulos, On the stability of the simple shear flow of a Johnson–Segalman fluid, [J. Non-Newtonian Fluid Mech.](#) **75**, 77 (1998).
- [69] M. M. Fyrillas, G. C. Georgiou, and D. Vlassopoulos, Time-dependent plane Poiseuille flow of a Johnson–Segalman fluid, [J. Non-Newtonian Fluid Mech.](#) **82**, 105 (1999).
- [70] J. Favero, A. Secchi, N. Cardozo, and H. Jasak, Viscoelastic flow analysis using the software OpenFOAM and differential constitutive equations, [J. Non-Newtonian Fluid Mech.](#) **165**, 1625 (2010).
- [71] A. F. Méndez-Sánchez, M. R. López-González, V. H. Rolón-Garrido, J. Perez-Gonzalez, and L. de Vargas, Instabilities of micellar systems under homogeneous and non-homogeneous flow conditions, [Rheol. acta](#) **42**, 56 (2003).
- [72] P. E. Boukany, Y. T. Hu, and S.-Q. Wang, Observations of wall slip and shear banding in an entangled DNA solution, [Macromolecules](#) **41**, 2644 (2008).
- [73] P. Tapadia and S.-Q. Wang, Direct Visualization of Continuous Simple Shear in Non-Newtonian Polymeric Fluids, [Phys. Rev. Lett.](#) **96**, 016001 (2006).
- [74] P. Tapadia and S.-Q. Wang, Yieldlike Constitutive Transition in Shear Flow of Entangled Polymeric Fluids, [Phys. Rev. Lett.](#) **91**, 198301 (2003).
- [75] M. Cromer, G. H. Fredrickson, and L. G. Leal, A study of shear banding in polymer solutions, [Phys. Fluids \(1994–present\)](#) **26**, 063101 (2014).
- [76] J. Adams and P. Olmsted, Nonmonotonic Models are not Necessary to Obtain Shear Banding Phenomena in Entangled Polymer Solutions, [Phys. Rev. Lett.](#) **102**, 067801 (2009).